

Determination of effective microscopic models for the frustrated antiferromagnets Cs_2CuCl_4 and Cs_2CuBr_4 by density functional methods

Kateryna Foyevtsova, Ingo Opahle, Yu-Zhong Zhang, Harald O. Jeschke, and Roser Valentí
Institut für Theoretische Physik, Goethe-Universität Frankfurt, 60438 Frankfurt am Main, Germany
(Dated: August 7, 2021)

We investigate the electronic and magnetic properties of the frustrated triangular-lattice antiferromagnets Cs_2CuCl_4 and Cs_2CuBr_4 in the framework of density functional theory. Analysis of the exchange couplings J and J' using the available X-ray structural data corroborates the values obtained from experimental results for Cs_2CuBr_4 but not for Cs_2CuCl_4 . In order to understand this discrepancy, we perform a detailed study of the effect of structural optimization on the exchange couplings of Cs_2CuCl_4 employing different exchange-correlation functionals. We find that the exchange couplings depend on rather subtle details of the structural optimization and that only when the insulating state (mediated through spin polarization) is present in the structural optimization, we do have good agreement between the calculated and the experimentally determined exchange couplings. Finally, we discuss the effect of interlayer couplings as well as longer-ranged couplings in both systems.

PACS numbers: 71.15.Mb,71.20.-b,75.10.Dg,75.10.Jm

I. INTRODUCTION

For almost two decades the frustrated antiferromagnets Cs_2CuCl_4 and Cs_2CuBr_4 have been considered as experimental realizations of a frustrated triangular lattice [1, 2]. Both systems crystallize in the space group $Pnma$ [3, 4] [see Fig. 1 (a)] and are characterized by a layered arrangement of Cu^{2+} ions in a triangular pattern parallel to the bc plane. The two-dimensional character of magnetic interactions between the spin- $\frac{1}{2}$ Cu^{2+} ions was confirmed by neutron scattering and susceptibility measurements in both systems [5–9] and was successfully modeled [10, 11] by a two-dimensional Heisenberg Hamiltonian containing an anisotropic interaction term of the Dzyaloshinskii-Moriya type [12, 13].

In spite of their structural similarity, Cs_2CuCl_4 and Cs_2CuBr_4 have rather different magnetic behavior. While in Cs_2CuBr_4 magnetic excitations are localized and the field dependent magnetization exhibits two well-defined plateaux [8], Cs_2CuCl_4 shows fractional spin excitations and spin liquid behavior over a broad temperature range, as revealed in inelastic neutron scattering experiments [5]. The dissimilar behavior between Cs_2CuCl_4 and Cs_2CuBr_4 has often been attributed to their unequal degree of frustration, determined as the ratio J'/J between the inter-chain exchange coupling J' and the dominant intra-chain exchange coupling J in the underlying triangular lattice [see Figs. 1 (b) and (c)].

A ratio of $J'/J = 0.74$ [15] has been suggested for Cs_2CuBr_4 by comparing the ordering vector of a helical incommensurate structure observed in neutron elastic scattering experiments with the one obtained from inverse temperature series expansions for a spin- $\frac{1}{2}$ Heisenberg model on an anisotropic triangular lattice [14]. In contrast, a ratio of $J'/J = 0.34$ [11] was derived for Cs_2CuCl_4 from comparison of spin-wave calculations for

the spin- $\frac{1}{2}$ Heisenberg model with the magnetic excitation spectrum observed in neutron scattering experiments in the presence of an external magnetic field far above saturation. These observations indicate that Cs_2CuCl_4 is less frustrated and more one-dimensional than Cs_2CuBr_4 .

While a large amount of work has been devoted to the description of the fractional quantum states and to understanding the phase transitions of the two-dimensional frustrated spin model with spatial anisotropy [16–34], a detailed comparative analysis of the electronic, magnetic and structural properties of these systems as well as a deep understanding of the origin of the different behavior is still missing.

In this work, we present an extensive density functional theory (DFT) study of the microscopic properties of Cs_2CuCl_4 and Cs_2CuBr_4 and compare our results with experimental data. We consider different exchange-correlation functionals in order to also investigate the dependence of the electronic, magnetic and structural properties on these choices. Our study of the performance of different exchange-correlation functionals is motivated by the fact that physical properties of recently discovered high temperature Fe-based superconductors are extremely sensitive to the details of DFT calculations [35–41]. Also, DFT studies of a recently topical layered Mott insulator TiOCl [42–51] reveals that it is essential to use a suitable exchange-correlation functional in DFT calculations to describe correctly the behavior of this system.

Out of the electronic structure calculations we derive a tight-binding (TB) Hamiltonian and estimate the Heisenberg exchange coupling constants between Cu ions from total energy calculations. Our DFT derived effective models incorporate a larger number of interacting Cu neighbors compared to the models used for the experimental data analysis. We show that some of these terms

are crucial for understanding the behavior of Cs_2CuCl_4 and Cs_2CuBr_4 .

II. STRUCTURAL AND ELECTRONIC PROPERTIES

(a) Structural optimization schemes

In this paper, we consider the experimentally measured structures of Cs_2CuCl_4 and Cs_2CuBr_4 as well as internal coordinates obtained from the structural optimization with various exchange-correlation functionals. The experimentally measured unit cell parameters of Cs_2CuCl_4 are taken from Ref. 3 and those of Cs_2CuBr_4 from Ref. 4. Both structures were measured at room temperature.

Crystal structure optimization of Cs_2CuCl_4 and Cs_2CuBr_4 is required since calculations with the experimentally determined structural parameters find quite large interatomic forces, which indicates that the structures are not in equilibrium within DFT. This holds for the calculations with all the considered exchange-correlation functionals listed below. In all cases, the interatomic forces are larger in Cs_2CuCl_4 compared to Cs_2CuBr_4 .

Based on our structural optimizations, we will discuss in detail the electronic properties of both compounds. For the structure optimization we apply the following schemes with different approximations to the exchange-correlation functional within DFT and different magnetic configurations: (1) the spin-independent local density approximation (LDA[nm]) [52]; (2) the spin-independent generalized gradient approximation (GGA[nm]) [53]; (3) the spin-dependent GGA with a ferromagnetic Cu spin configuration (GGA[fm]); (4) the spin-dependent GGA+U [55] with a ferromagnetic Cu spin configuration (GGA+U[fm]). For the GGA+U[fm] calculations we considered the around mean field (AMF) version [56] with values of U and J_H for the Cu ions of 6 eV and 1 eV respectively. The lattice constants, which are assumed to be well determined from experiments, were kept fixed for the structure relaxations while the optimization of the relative atomic positions was constrained by the symmetry of the $Pnma$ space group.

For Cs_2CuCl_4 , we also considered two optimization schemes with an antiferromagnetic Cu spin configuration: GGA[afm] and GGA+U[afm] ($U = 6$ eV, $J_H = 1$ eV). The spin arrangement in this antiferromagnetic configuration is shown in Fig. 1 (d), where the Cs_2CuCl_4 unit cell was doubled in the b direction along the Cu chains. In order to produce such an arrangement, the symmetry of the supercell was lowered to the space group $P21/c$, with two inequivalent Cu atoms. Our choice of this particular antiferromagnetic configuration is due to its resemblance to the experimentally observed 120° ground state configuration [57]. The considered antiferromagnetic configuration

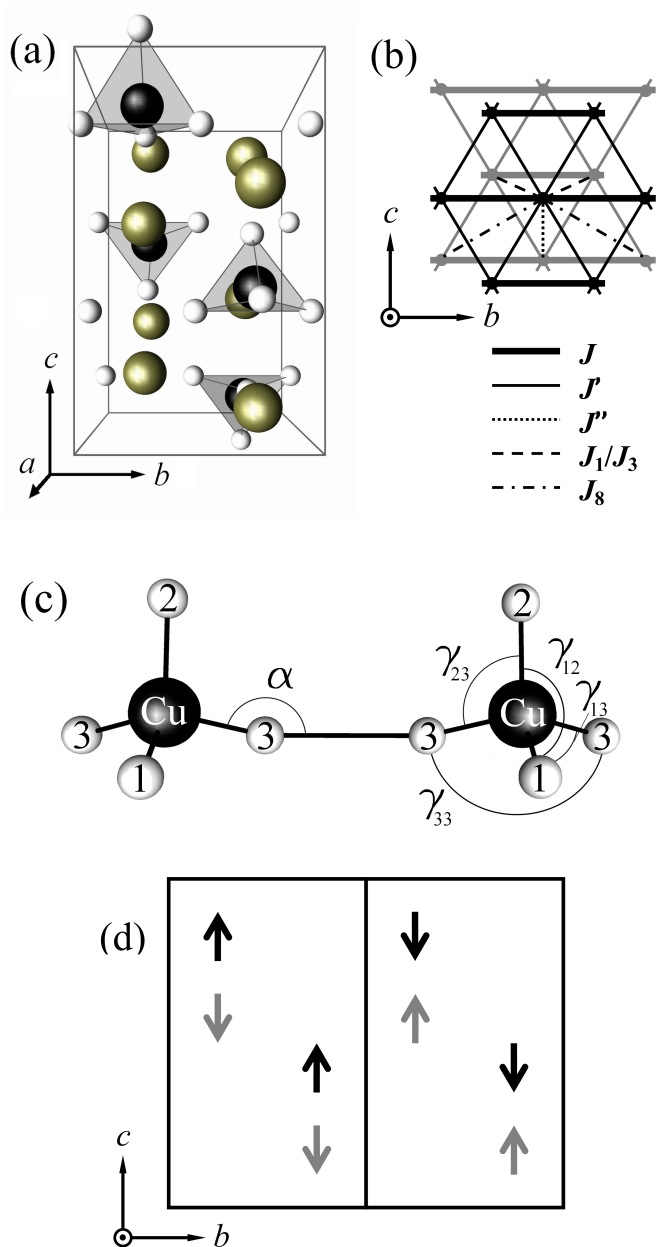


FIG. 1: (Color online) (a) The Cs_2CuCl_4 and Cs_2CuBr_4 unit cell where the CuX_4 tetrahedra ($X = \text{Cl}, \text{Br}$) are highlighted. (b) Schematic triangular lattice of Cu spins. The gray lattice is below the black lattice. (c) Neighboring CuX_4 tetrahedra. Labels 1, 2 and 3 of the X atoms denote the three inequivalent X atoms: $X(1)$, $X(2)$ and $X(3)$. As indicated, angles γ_{12} , γ_{13} correspond to the angles $X(1)\text{-Cu-}X(2)$, $X(1)\text{-Cu-}X(3)$, etc. (d) Cu spin configuration of a $1 \times 2 \times 1$ supercell of Cs_2CuCl_4 adopted for the structural optimization within the GGA+U[afm] scheme.

is collinear, which is beneficial in terms of computational effort, and fulfills the requirement that the strongest couplings J are satisfied and the second strongest couplings J' are partially satisfied. The optimization of the relative atomic positions with the two antiferromagnetic schemes was constrained by the symmetry of the $P21/c$ space group.

Additionally, for both systems we completed the LDA series of structural optimizations with LDA[fm] and LDA+U[fm] optimizations. However, due to the analogous behavior of the structural properties of Cs_2CuCl_4 and Cs_2CuBr_4 observed within this series with those within the GGA series, the detailed analysis of the LDA series will be omitted here.

The DFT structural optimizations were performed with the full-potential local-orbital (FPLO) code [61, 67] in the scalar relativistic approximation with up to 512 \mathbf{k} -points in the full Brillouin zone.

(b) Band gap

Before presenting the structure optimizations with the different exchange-correlation functionals, we shall consider the experimental crystal structure and discuss the electronic properties obtained with the different exchange-correlation functionals. Calculations with the GGA[nm], GGA[fm] or GGA+U[fm] exchange-correlation potentials result in the electronic structure being either gapless (GGA[nm]) or gapped (GGA[fm] and GGA+U[fm]), as shown in Fig. 2. Allowing for spin polarization opens a gap in both Cs_2CuCl_4 and Cs_2CuBr_4 [though in the latter compound the GGA[fm] gap is rather small (~ 0.03 eV)]. Upon introducing the onsite Coulomb repulsion within the GGA+U[fm], the gaps in both systems increase considerably [Fig. 2 (c) and (f)].

Spin-dependent exchange-correlation functionals provide a better description of Cs_2CuCl_4 and Cs_2CuBr_4 electronic properties as these functionals correctly reproduce the experimentally observed insulating ground state of the compounds. Moreover, as it will be shown in the next sections, it turns out that the presence of a band gap is important for the accurate determination of the equilibrium crystal structures.

(c) Structural analysis

We proceed now with the structural optimization. The crystal structures of Cs_2CuCl_4 and Cs_2CuBr_4 resulting after optimization with each of the schemes described above are presented in Appendix A. In our analysis of these structures we focus on geometry variations of the CuX_4 ($X = \text{Cl}, \text{Br}$) tetrahedron, which determine the strength of important exchange couplings.

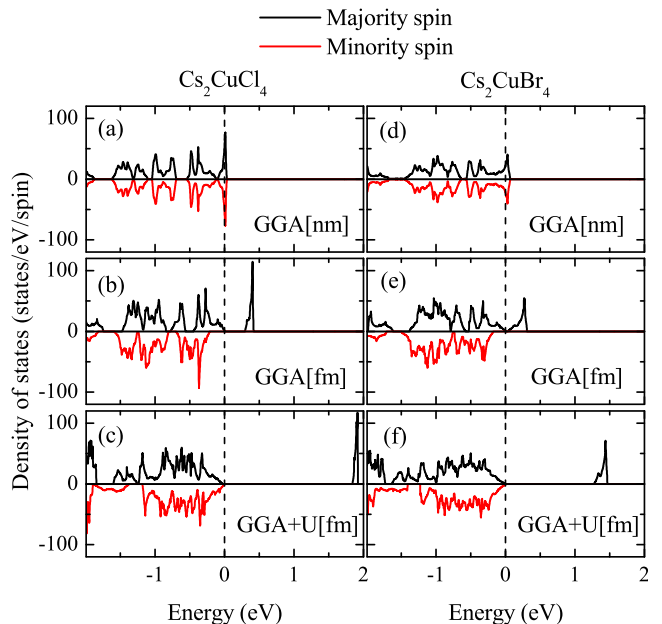


FIG. 2: (Color online) Total densities of states for majority and minority electron spin for (a) Cs_2CuCl_4 , calculated with GGA[nm], (b) Cs_2CuCl_4 , calculated with GGA[fm], (c) Cs_2CuCl_4 , calculated with GGA+U[fm], (d) Cs_2CuBr_4 , calculated with GGA[nm], (e) Cs_2CuBr_4 , calculated with GGA[fm], and (f) Cs_2CuBr_4 , calculated with GGA+U[fm]. For an easier comparison, the two DOS's are plotted with opposite signs. The calculations are performed with the LAPW code Wien2k [see Section II (d)]. In the case of GGA+U[fm], the around mean field scheme is employed, with $U = 6$ eV and $J_{\text{H}} = 1$ eV. The Fermi level is set to zero.

In Cs_2CuCl_4 and Cs_2CuBr_4 , the CuX_4 tetrahedron is distorted due to the Jahn-Teller effect and also due to the steric pressure originating from Cs^+ ions [4]. The Jahn-Teller effect results in a squeezing of the tetrahedron such that the $X\text{-Cu-X}$ bond angles γ_{12} and γ_{33} increase and the $X\text{-Cu-X}$ bond angles γ_{13} and γ_{23} decrease [Fig. 1 (c)]. The steric pressure by $\text{Cs}(2)$ on $X(3)$ causes additional symmetry lowering by increasing γ_{13} and decreasing γ_{33} . In order to compare the strengths of the two types of distortions in different structures, one can define the Jahn-Teller deviation Δ^{JT} as the difference between averages $\frac{1}{2}(\gamma_{12} + \gamma_{33})$ and $\frac{1}{2}(\gamma_{13} + \gamma_{23})$,

$$\Delta^{\text{JT}} = \left| \frac{1}{2}(\gamma_{12} + \gamma_{33}) - \frac{1}{2}(\gamma_{13} + \gamma_{23}) \right|, \quad (1)$$

and the steric pressure deviations δ_1^{steric} and δ_2^{steric} as

$$\delta_1^{\text{steric}} = \frac{\frac{1}{2}|\gamma_{12} - \gamma_{33}|}{\frac{1}{2}(\gamma_{12} + \gamma_{33})} \quad \text{and} \quad \delta_2^{\text{steric}} = \frac{\frac{1}{2}|\gamma_{13} - \gamma_{23}|}{\frac{1}{2}(\gamma_{13} + \gamma_{23})}. \quad (2)$$

As can be seen in Appendix A, the Cs_2CuCl_4 structures relaxed with GGA[fm] and GGA[afm] are very close as well as the structures relaxed with GGA+U[fm]

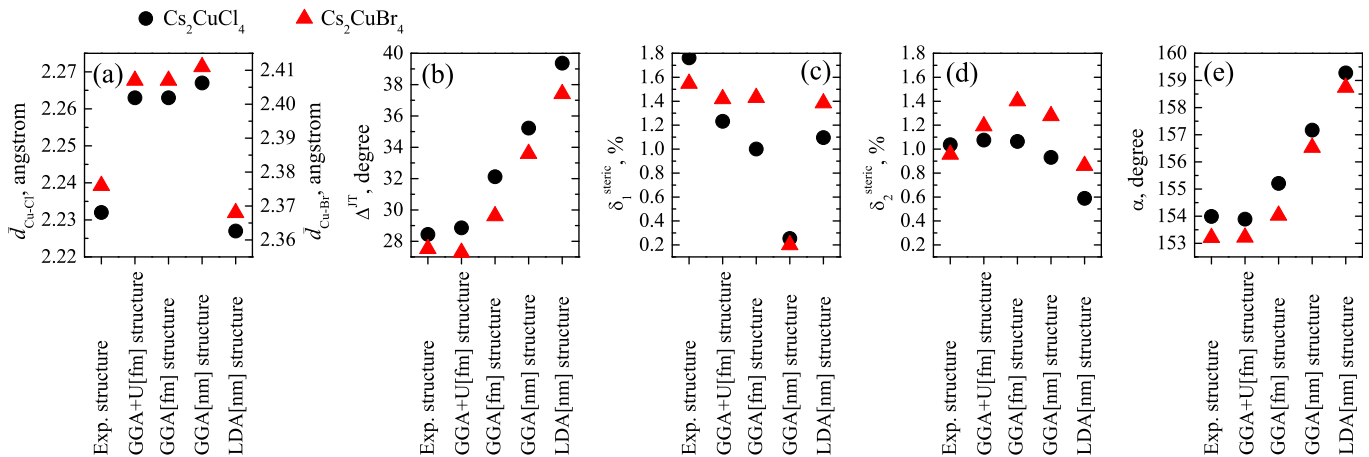


FIG. 3: (Color online) (a) The average Cu- X ($X = \text{Cl}, \text{Br}$) bond distance $\bar{d}_{\text{Cu}-X}$, (b) Jahn-Teller deviation Δ^{JT} , (c) steric pressure deviation δ_1^{steric} , (d) steric pressure deviation δ_2^{steric} and (e) Cu- X - X angle α in the J superexchange bridge in the experimental as well as relaxed Cs_2CuCl_4 and Cs_2CuBr_4 crystal structures.

and GGA+U[afm]. The tetrahedron parameters in these structures are also similarly close. This demonstrates that, within the spin-dependent GGA and GGA+U, interatomic forces in Cs_2CuCl_4 are very weakly dependent on the actual Cu spin configuration and in the following we will consider only ferromagnetic spin-dependent relaxation schemes for Cs_2CuCl_4 and Cs_2CuBr_4 . This result is a consequence of the rather small energy scale of magnetic interactions between Cu spins, which is much smaller than the difference between total energies usually involved in structural relaxations.

In Tables I and II, we present the tetrahedron parameters defined above for the experimental and relaxed crystal structures of Cs_2CuCl_4 and Cs_2CuBr_4 , respectively. Some of them are additionally shown in Fig. 3 in order to facilitate the comparison of the different crystal structures. In both compounds, the crystal structures of the GGA relaxation series (GGA+U[fm], GGA[fm] and GGA[nm]) are featured by a continuous variation of the X -Cu- X angles. In terms of these angles, the relaxed crystal structures closest to the experimental structures are the GGA+U[fm] structures for both Cs_2CuCl_4 and Cs_2CuBr_4 . However, in terms of Cu- X bond distances, represented here as the averaged distance $\bar{d}_{\text{Cu}-X}$, the GGA crystal structures are further away from the experimental structures than the LDA structures [see Fig. 3 (a)]. In the LDA structures (including the LDA[fm] and LDA+U[fm] ones, which are not listed in the tables), $\bar{d}_{\text{Cu}-X}$ are smaller than the corresponding parameters of the experimental structures, but the difference is less compared to the GGA series. Thus, the GGA relaxation tends to increase the bond distances in the CuX_4 tetrahedron while the LDA relaxation decreases them.

In the GGA series, the Jahn-Teller-like distortion of the tetrahedron, which we evaluate through Δ^{JT} , is

TABLE I: Tetrahedron parameters for the Cs_2CuCl_4 structures and corresponding values of the Cu magnetic moment during structural relaxation. The angles are given in degrees, the deviations δ_1^{steric} and δ_2^{steric} in percent and the averaged Cu-Cl distance $\bar{d}_{\text{Cu}-\text{Cl}}$ in Ångström.

	exp	GGA+U[fm]	GGA[fm]	GGA[nm]	LDA[nm]
γ_{12}	131.33	130.97	133.05	133.66	135.56
γ_{13}	101.67	101.60	100.67	99.69	98.26
γ_{23}	99.58	99.43	98.55	97.86	97.11
γ_{33}	126.79	127.78	130.41	134.34	138.56
Δ^{JT}	28.44	28.86	32.12	35.22	39.38
α	153.99	153.89	155.21	157.17	159.28
δ_1^{steric}	1.76	1.23	1.00	0.25	1.10
δ_2^{steric}	1.04	1.08	1.06	0.93	0.59
$\bar{d}_{\text{Cu}-\text{Cl}}$	2.232	2.263	2.263	2.267	2.227
μ	-	$0.78\mu_B$	$0.50\mu_B$	0	0

strongest in the GGA[nm] crystal structures of both compounds and decreases monotonically as the Cu magnetic moment in the spin-resolved calculations increases (GGA[fm], GGA+U[fm]) [see Fig. 3 (b)]. The Cu magnetic moment in Cs_2CuCl_4 calculated with either GGA[fm] or GGA[afm] schemes is $0.50\mu_B$ and increases to $0.78\mu_B$ when the onsite Coulomb interaction is switched on within the GGA+U functional (Table I). In Cs_2CuBr_4 , the corresponding values of the Cu magnetic moment are $0.42\mu_B$ and $0.73\mu_B$ [58] (Table II). In the LDA[nm] structures, Δ^{JT} takes the largest value. The distortion due to steric pressure, which is characterized by δ_1^{steric} and δ_2^{steric} [Figs. 3 (c) and (d)], does not appear to follow any general rule.

For the further discussion of the electronic structure it

TABLE II: Tetrahedron parameters for the Cs_2CuBr_4 structures and corresponding values of the Cu magnetic moment during structural relaxation. The angles are given in degrees, the deviations δ_1^{steric} and δ_2^{steric} in percent and the averaged Cu-Br distance $\bar{d}_{\text{Cu-Br}}$ in Ångström.

	exp	GGA+U[fm]	GGA[fm]	GGA[nm]	LDA[nm]
γ_{12}	130.40	130.06	131.77	132.53	133.72
γ_{13}	102.16	102.16	101.70	100.48	99.03
γ_{23}	99.93	99.75	98.89	97.94	97.34
γ_{33}	126.42	126.42	128.05	133.07	137.48
Δ^{JT}	27.52	27.28	29.62	33.59	37.41
α	153.21	153.22	154.03	156.53	158.74
δ_1^{steric}	1.55	1.42	1.43	0.20	1.38
δ_2^{steric}	0.96	1.19	1.40	1.28	0.86
$\bar{d}_{\text{Cu-Br}}$	2.376	2.407	2.407	2.411	2.368
μ	-	$0.73\mu_B$	$0.42\mu_B$	0	0

is useful to consider an additional structural parameter, namely, the angle in the J superexchange bridge Cu- X - X -Cu, shown in Fig. 1 (c) as α . This angle is closely related to γ_{33} and behaves analogously in the various structures [see Fig. 3 (e) and Tab. I]. The large variation of the superexchange coupling J in different Cs_2CuCl_4 relaxed crystal structures is mainly attributed to the variation of α , as will be discussed in Section III.

(d) Electronic structure

In this section, we present a detailed analysis of electronic properties of Cs_2CuCl_4 and Cs_2CuBr_4 for the experimental and relaxed crystal structures introduced in the previous section. We show the results obtained with the spin-independent GGA exchange-correlation functional as these are also used for the tight-binding parametrization. Calculations were performed with both the FPLO code as well as the linearized augmented plane wave (LAPW) scheme, as implemented in the Wien2k code [59]. The calculations with both codes are in good agreement and the data presented here are obtained with the LAPW code.

Fig. 4 displays the density of states (DOS) for Cs_2CuCl_4 and Cs_2CuBr_4 obtained using the experimental structure. In both compounds, the hybridized Cu $3d$ and Cl $3p$ /Br $4p$ bands occupy the energy range between about -4 eV and 0 eV [see, for instance, the atomic DOS in Figs. 4 (a) and (c)]. At the Fermi level, the Cu $3d_{xy}$ states are half-filled as Cu is in a $3d^9$ configuration. There are four Cu $3d_{xy}$ bands in the bandstructure, which corresponds to the number of Cu atoms per unit cell. A gap of approximately 4 eV separates the Cu and X ($X = \text{Cl}, \text{Br}$) bands from the next unoccupied states [not shown in Figs. 4 (a) and (c)], which have significant Cs contribu-

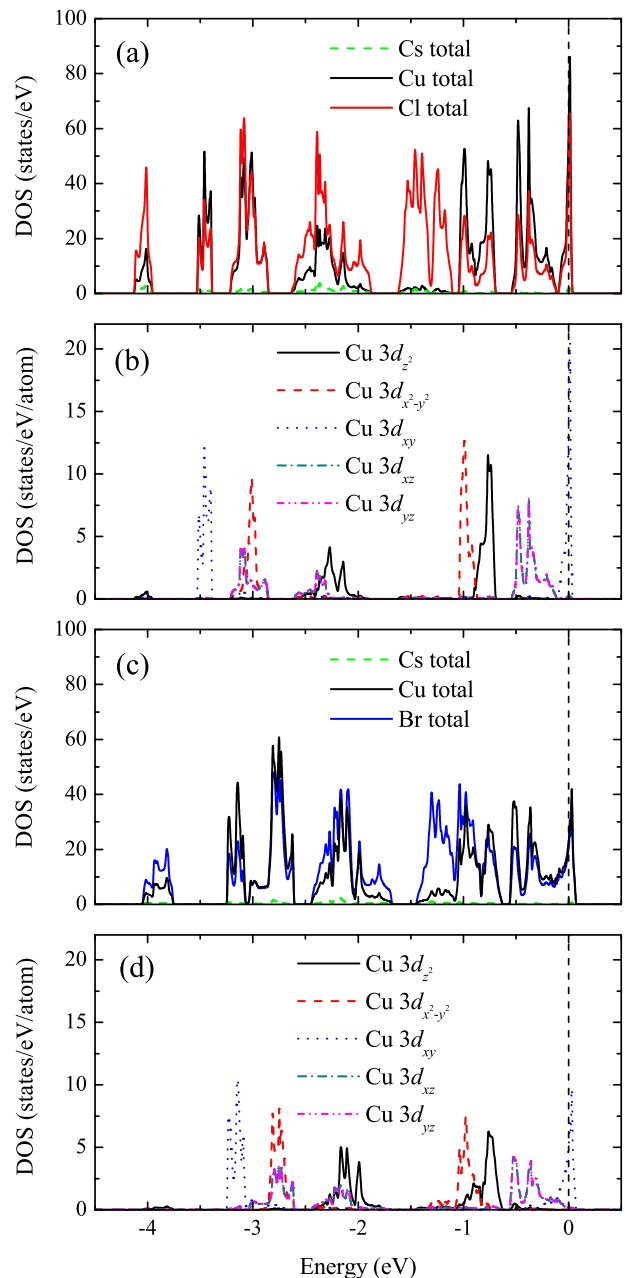


FIG. 4: (Color online) Atomic species resolved densities of states (DOS) calculated from the experimental crystal structures for (a) Cs_2CuCl_4 and (c) Cs_2CuBr_4 and the orbital projected densities of states of Cu $3d$ for (b) Cs_2CuCl_4 and (d) Cs_2CuBr_4 . Energy is measured relative to the Fermi level E_F .

tion.

Almost no contribution from Cs atoms to the DOS near the Fermi level is observed indicating a negligible hybridization of Cu with Cs. In particular, this indicates that exchange coupling J along the Cu chains in the b direction arises from the Cu- X - X -Cu hybridization.

The Cu and X band manifold is an assembly of bonding states in the interval between -4 eV and -2 eV and

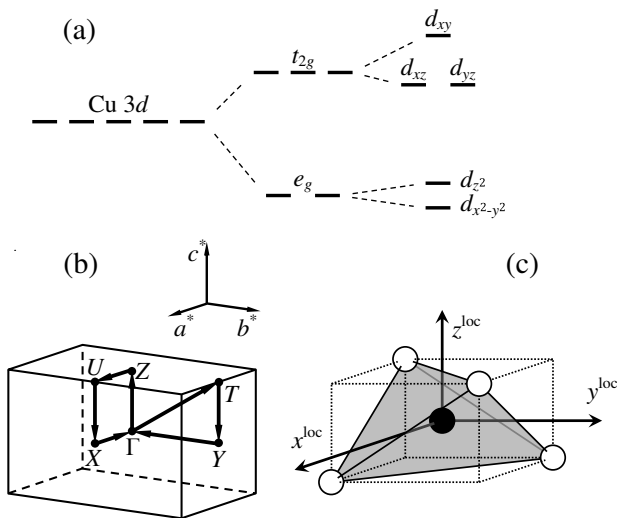


FIG. 5: (a) A schematic splitting of Cu 3d orbitals in the crystal field. (b) The path in the $\text{Cs}_2\text{CuCl}_4/\text{Cs}_2\text{CuBr}_4$ Brillouin zone for bandstructure calculations (Figs. 6 and 7). (c) The local reference frame of a Cu atom, in which its orbital projected density of states is defined.

antibonding states in the interval from -2 eV up to the Fermi level. The Cu antibonding states are split by the crystal field generated by X^- ions surrounding a Cu^{2+} ion into the energetically lower Cu e_g doublet ($d_{x^2-y^2}$ and d_{z^2}) and the energetically higher Cu t_{2g} triplet (d_{xy} , d_{xz} and d_{yz}). Due to the Jahn-Teller-like uniaxial distortion of the tetrahedron, the t_{2g} triplet is further split into the degenerate d_{xz}/d_{yz} states and the half-filled d_{xy} states. This splitting is schematically illustrated in Fig. 5 (a), and the orbital projected densities of Cu 3d states for the experimental Cs_2CuCl_4 and Cs_2CuBr_4 structures are presented in Figs. 4 (b) and (d), respectively. Note that the orbital designation is given according to the local reference frame of the CuX_4 tetrahedron as shown in Fig. 5 (c).

In Figs. 6 and 7, we present the total DOS and bandstructures for the experimental as well as relaxed crystal structures (GGA+U[fm], GGA[fm], GGA[nm], LDA[nm]) of Cs_2CuCl_4 and Cs_2CuBr_4 , respectively. In contrast to Cs_2CuCl_4 , the t_{2g} states in Cs_2CuBr_4 are strongly hybridizing, which is indicated by the non-separable character of the overlap of the Cs_2CuBr_4 d_{xy} and d_{xz}/d_{yz} bands in the bandstructure.

We now focus on the comparison between the electronic structures of Cs_2CuCl_4 and Cs_2CuBr_4 calculated from different crystal structures. In both compounds, the choice of the relaxation scheme determines the degree of separation between the d_{xy} and d_{xz}/d_{yz} bands and the dispersion of the d_{xy} band. The separation between the d_{xy} and d_{xz}/d_{yz} bands is reduced in the GGA[nm] crystal structure, compared to the LDA[nm] one, and

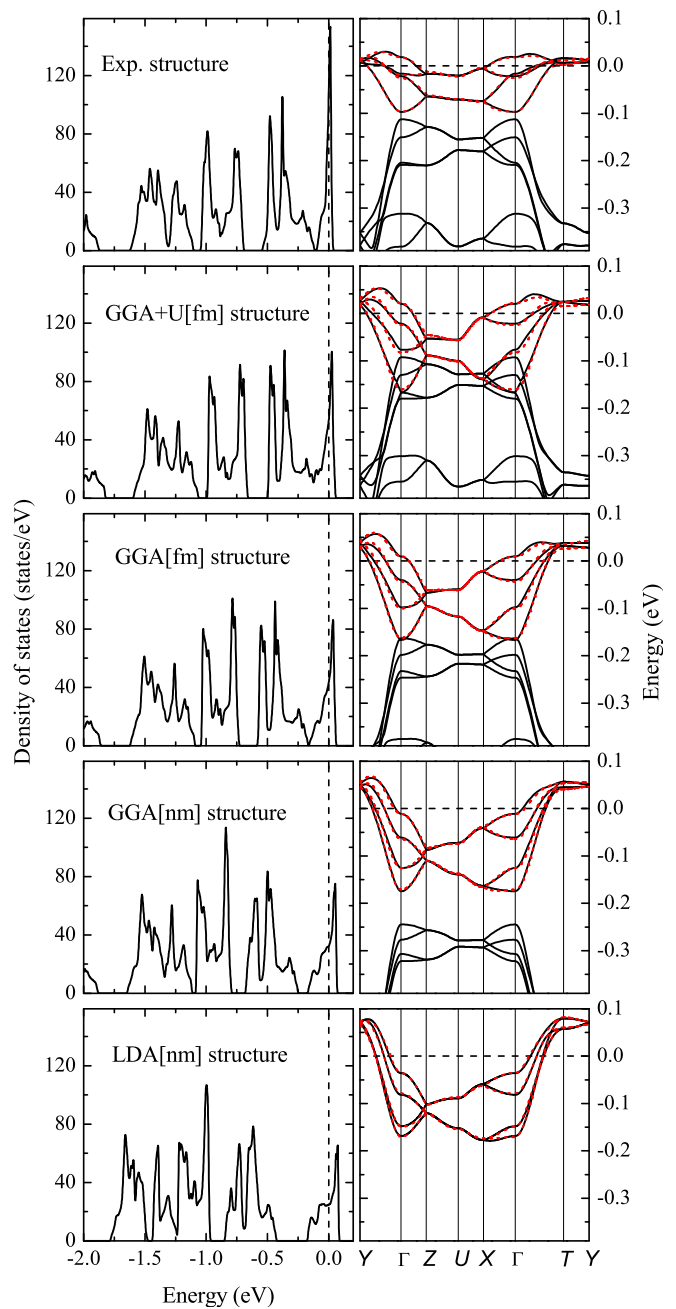


FIG. 6: (Color online) DOS and bandstructures for various Cs_2CuCl_4 structures (specified by the panel captions). In the bandstructure plots, the DFT calculated bands are in black (solid) lines and the tight-binding fits are in red (dashed) lines. The bandstructure path in the Brillouin zone is shown in Fig. 5 (b). Energy is again measured relative to the Fermi level E_F .

keeps reducing within the GGA series as the value of the Cu magnetic moment, associated with a given relaxation functional, gets larger (GGA[fm], GGA+U[fm]). This trend is better seen in Cs_2CuCl_4 where the d_{xy} band is separated by a gap (except for the GGA+U[fm] struc-

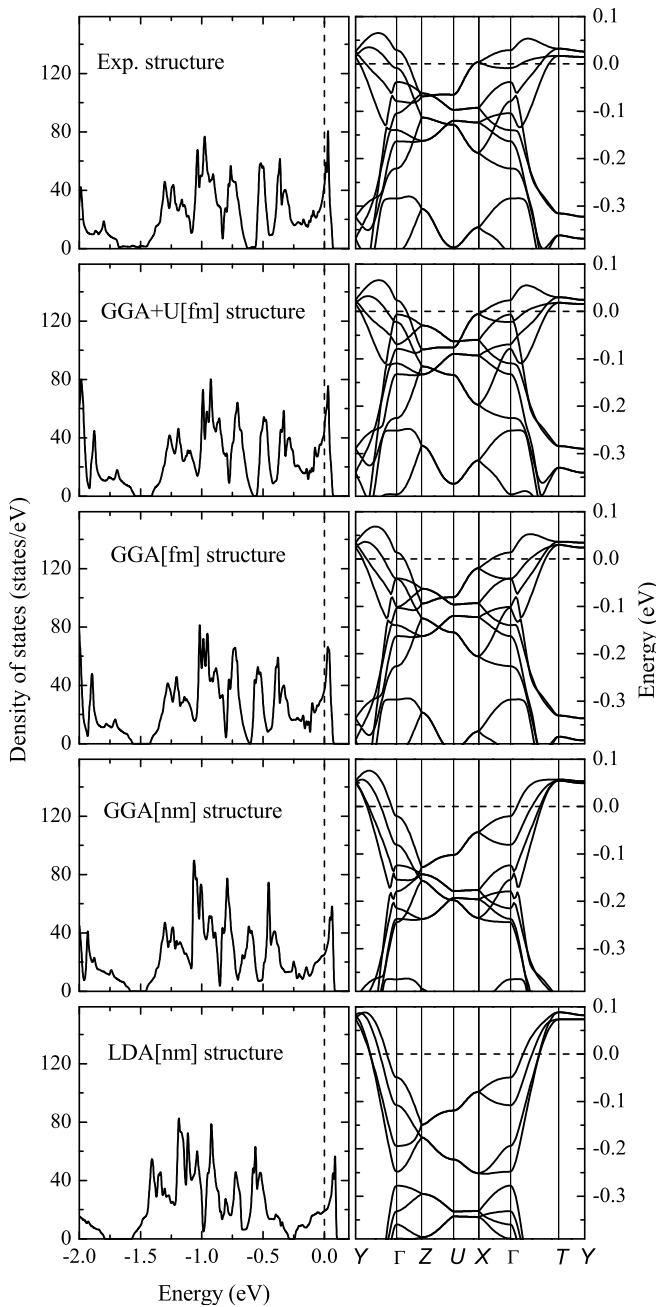


FIG. 7: DOS and bandstructures of various Cs_2CuBr_4 structures (specified by the panel captions). The bandstructure path in the Brillouin zone is shown in Fig. 5 (b).

ture). We relate the variation of the degree of separation to the variation of the Jahn-Teller-like distortion of the CuX_4 tetrahedron. Our assumption is supported by the structural analysis in Tables I and II as one observes there that the structures possessing more distorted tetrahedra demonstrate larger d_{xy} and d_{xz}/d_{yz} band separation in the electronic structure.

Analysis of the d_{xy} band dispersion shows that the

d_{xy} bandwidth does not change significantly among the Cs_2CuBr_4 structures including the experimental one (Fig. 7). In Cs_2CuCl_4 , the d_{xy} bandwidth of the experimental crystal structure is significantly narrower compared to that of the relaxed crystal structures, where it stays nearly uniform (Fig. 6). The shape of the d_{xy} bands varies in details from structure to structure in both compounds. This shape variation is accompanied by a variation of the density of states distribution within the d_{xy} orbital, which is easier to quantify. Thus, in both compounds, the weight of the d_{xy} DOS gets shifted closer to the Fermi energy in the LDA[nm], GGA[nm], GGA[fm], GGA+U[fm] crystal structures sequence, which results in a more peaked appearance of the d_{xy} DOS. The DOS at the Fermi level increases correspondingly. In the experimental Cs_2CuCl_4 structure, the DOS at the Fermi level is extremely sharp also due to the flatness of the d_{xy} band.

(e) TB model for Cs_2CuCl_4

The changes observed among the various electronic structures of Cs_2CuCl_4 and Cs_2CuBr_4 can also be discussed on a quantitative level by mapping bandstructures to a tight-binding (TB) Hamiltonian:

$$H^{\text{TB}} = \mu \sum_i \hat{c}_{i,\sigma}^\dagger \hat{c}_{i,\sigma} - \sum_{\substack{\langle i,j \rangle, \sigma \\ i \neq j}} \left(t_{ij} \hat{c}_{i,\sigma}^\dagger \hat{c}_{j,\sigma} + \text{h. c.} \right), \quad (3)$$

where $\hat{c}_{i,\sigma}^\dagger$ and $\hat{c}_{i,\sigma}$ are, respectively, the creation and annihilation operators of electrons on site i and with spin σ , t_{ij} denotes the hopping integrals and h. c. denotes Hermitian conjugate terms.

Since in Cs_2CuCl_4 the Cu $3d_{xy}$ bands at the Fermi level are well separated from the rest of the t_{2g} manifold, its low-energy properties can be described by a one-band TB model. The hopping integrals are evaluated by Fourier-transforming the Hamiltonian Eq. (3) and mapping its eigenvalues to the four DFT Cu $3d_{xy}$ bands.

In Cs_2CuBr_4 , the TB procedure is complicated by the hybridization of the overlapping d_{xy} and d_{xz}/d_{yz} bands. In this case, a three-band TB model is required. Since the three-band TB model includes new electronic degrees of freedom due to electron hopping between different types of orbitals, the number of independent hopping integrals in this model is considerably larger, compared to the one-band case. With an increasing number of model parameters, the TB parametrization by means of fitting becomes less reliable, and therefore we do not apply this method to Cs_2CuBr_4 in the present work. The rest of this section will be dedicated to the discussion of the Cs_2CuCl_4 single-band TB models.

Though it was experimentally established [11] that the spin interactions in Cs_2CuCl_4 are predominantly within

TABLE III: The TB model parameters in meV for the Cs_2CuCl_4 Cu $3d_{xy}$ band, calculated from the various Cs_2CuCl_4 crystal structures. The hopping integral index corresponds to the order of the neighbor. The less important interaction pathways, not present in Fig. 1 (b), are shown in Fig. 9 (a) (Appendix B).

	LDA[nm]	GGA[nm]	GGA[fm]	GGA+U[fm]	exp.
t	-44.9	-35.9	-27.4	-21.7	-11.0
t'	12.5	-13.6	14.0	14.4	6.7
t''	-1.4	-4.5	-6.0	-6.8	-6.3
t_1	6.3	-7.4	-6.3	-3.6	-3.9
t_3	-9.5	8.4	7.5	7.5	8.2
t_7	2.4	2.3	2.6	2.9	2.3
t_8	-2.2	-2.5	-2.7	-3.0	3.6
t_6	-2.4	-2.8	-3.0	-2.7	1.7
t_{14}	0.6	0.9	1.1	1.4	1.6
t_{18}	0.0	0.2	0.3	0.6	-0.1
t_{22}	-4.8	-5.1	-4.5	-4.4	-2.4
μ	-15.3	-17.3	-17.6	-17.8	-11.7

the Cu layer along the J and J' paths [see Fig. 1 (b)], we observe that the electronic behavior modeled by the TB Hamiltonian show non-negligible interlayer hopping terms. We find that the d_{xy} bands of all the Cs_2CuCl_4 structures can only be satisfactorily described with a minimal model that includes five hopping integrals. Three of them are the intralayer hoppings t and t' and the interlayer hopping t'' (t , t' , t'' correspond to the interaction paths J , J' , J'' , etc.), which have been considered in previous studies in the framework of spin Hamiltonians. The two new hopping parameters are the interlayer t_1 and t_3 , also shown in Fig. 1 (b), their indices indicating the order of the interacting Cu neighbor. Note that t , t' and t'' as well as J , J' and J'' correspond to fifth, fourth and second nearest neighbour in the structure, respectively, while for all other t_i and J_i the index corresponds to the order of the neighbour. In Table III, we present the values of relevant hopping integrals for the various Cs_2CuCl_4 structures. We observe that t_1 and t_3 are in many cases comparable in magnitude to the hopping integral t' . We also note that the presence of non-negligible interlayer couplings is revealed by a significant dispersion of the d_{xy} bands along the a^* direction in k -space (the $X - \Gamma$ path in Fig. 6). Additionally, we confirmed the importance of t_1 and t_3 by performing NMTO downfolding calculations [60] for some of the relaxed crystal structures.

The total number of TB hopping integrals considered for an accurate description of the DFT bandstructure of Cs_2CuCl_4 amounts to 11, plus the onsite energy μ (Table III). Fig. 6 displays in dashed red lines the TB fit to the DFT Cu $3d_{xy}$ bands, which are in solid black lines. Interaction pathways for the first seven hopping integrals are shown schematically in Figs. 1 (b) and 9 (a) (in Appendix A).

Comparing the TB models for different Cs_2CuCl_4

structures, we observe that the dominant hopping integral t has the smallest absolute value for the experimental crystal structure and increases in the GGA crystal structure series with a decrease of the Cu magnetic moment during relaxation (GGA+U[fm], GGA[fm], GGA[nm]). It has a maximum value in the LDA[nm] structure. At the same time, the second important coupling t' does not change significantly among the relaxed structures, but is by a factor of two smaller in the experimental crystal structure. The interlayer coupling t_3 is stable for all the structures, while t'' and t_1 vary considerably.

We associate the variation of the hopping integral t in different Cs_2CuCl_4 crystal structures with the variation of the CuCl_4 tetrahedron geometry and, in particular, with the variation of the angle α in the Cu-Cl(3)-Cl(3)-Cu interaction path. In the relaxed Cs_2CuCl_4 crystal structures, larger t values correspond to larger values of α and larger tetrahedron distortions. However, the experimental structure does not follow this rule; while the angles of the experimental and GGA+U[fm] relaxed structures are very similar, the t values differ by a factor of two. The reason why the experimental structure deviates from the relaxed structures might be the influence of other tetrahedron parameters, such as details of the Cu-Cl bond distances.

The observed relation between the dominant hopping integral t and the angle α is reasonable since α is the defining angle for the Cu $3d_{xy}$ -Cl $3p$ -Cl $3p$ -Cu $3d_{xy}$ hybridization. By considering perturbation theory on the onsite Coulomb repulsion U up to the second order, the effective Cu-Cu superexchange coupling can be obtained from t as $J = \frac{4t^2}{U}$. Then, the relation between t and α fulfills the Kanamori-Goodenough rule [62, 63], stating that J reaches a maximum when the cation-anion-cation angle equals 180° . In the present case of the cation-anion-anion-cation (Cu-Cl-Cl-Cu) bridge, the four atoms get aligned along a straight line when α increases.

III. EXCHANGE INTEGRALS

(a) Computational details

The exchange coupling integrals J_{ij} of the Heisenberg Hamiltonian,

$$H_{\text{H}} = \sum_{\langle i,j \rangle} J_{ij} \mathbf{S}_i \mathbf{S}_j, \quad (4)$$

can be obtained by means of DFT spin-resolved total energy calculations [64]. Considering the differences between the energies of the ferromagnetic configuration and various antiferromagnetic spin configurations, $E^{\text{FM}} - E_i^{\text{AFM}}$, one derives a set of coupled equations for the couplings J_{ij} . Following Eq. (4), antiferromagnetic exchange corresponds to positive J_{ij} .

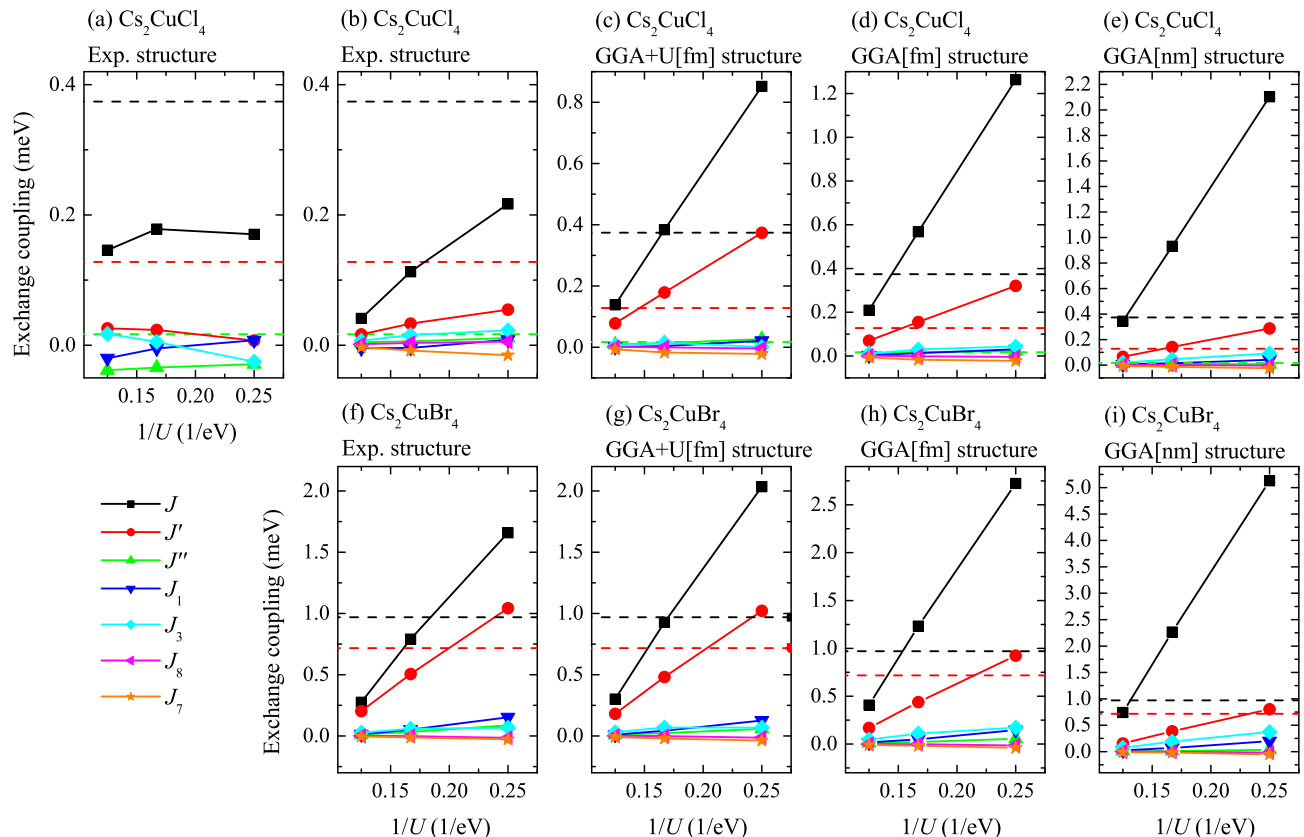


FIG. 8: (Color online) The spin exchange coupling constants as functions of $1/U$ for (a) the Cs_2CuCl_4 experimental structure calculated with the atomic limit version of the GGA+U, (b) the Cs_2CuCl_4 experimental structure (c) the Cs_2CuCl_4 GGA+U[fm] relaxed structure, (d) the Cs_2CuCl_4 GGA[fm] relaxed structure, (e) the Cs_2CuCl_4 GGA[nm] relaxed structure, (f) the Cs_2CuBr_4 experimental structure, (g) the Cs_2CuBr_4 GGA+U[fm] relaxed structure, (h) the Cs_2CuBr_4 GGA[fm] relaxed structure, (i) the Cs_2CuBr_4 GGA[nm] relaxed structure. When not specified otherwise, the exchange couplings are obtained with the around mean field version of the GGA+U. The three sets of exchange couplings correspond to $U = 8, 6$ and 4 eV. Dashed lines mark the experimentally determined values of J, J' and J'' .

For Cs_2CuCl_4 and Cs_2CuBr_4 , we take into account seven important couplings corresponding to the first seven hopping integrals in Table III, which are $J, J', J''_{\text{eff}} = J'' + J_6, J_1, J_3, J_7$ and J_8 [see Figs. 1 (b) and 9 (a)]. This choice defines the number of antiferromagnetic configurations to be calculated. The combined coupling J''_{eff} is introduced because the considered unit cell (which is a $2 \times 2 \times 1$ supercell) does not allow a separate calculation of the couplings J'' and J_6 but only their calculation as a sum. Since J'' is presumably larger than J_6 , J''_{eff} gives an approximate value of J'' .

The choice of the supercell is dictated by the peculiarities of the Cs_2CuCl_4 and Cs_2CuBr_4 magnetic sublattices. First, since the candidate for the largest coupling J connects Cu atoms that belong to adjacent primitive unit cells in Cs_2CuCl_4 and Cs_2CuBr_4 , the primitive unit cell has to be doubled in the b direction. Otherwise, J would be always canceled in any $E^{\text{FM}} - E_i^{\text{AFM}}$ difference. Also, in order to be able to discern the inequivalent couplings J_1 and J_3 , we double the unit cell once more in the a di-

rection and thus end up with a $2 \times 2 \times 1$ supercell. In the supercell, we set eight out of 16 Cu atoms inequivalent in order to be able to arrange the required seven antiferromagnetic configurations within the same unit cell space group, which is $P-1$. It is important to stay within the same space group during total energy calculations for Cs_2CuCl_4 and Cs_2CuBr_4 as in these compounds the exchange couplings are small and integration over differently sampled Brillouin zones can affect the accuracy of the results.

The seven antiferromagnetic spin configurations, together with the set of coupled equations for the exchange couplings, are presented in Appendix C. The total energy calculations were performed with the FPLO code. Test calculations with Wien2k confirm the results. In the FPLO code, we chose a $5 \times 4 \times 3$ mesh of k -points for the supercell Brillouin zone integration and kept other settings at default. The scheme to compute magnetic exchange for a given structure consisted of a series of total energy calculations within the AMF version of the

GGA+U, with $U = 4, 6$ and 8 eV and $J_H = 1$ eV in all cases. This scheme was applied to the experimental structures of Cs_2CuCl_4 and Cs_2CuBr_4 and also to the GGA[nm], GGA[fm] and GGA+U[fm] relaxed structures of the two compounds.

(b) Results

The calculated exchange couplings are plotted in Fig. 8, as a function of $1/U$. For an easy comparison, we also mark by horizontal dashed lines of corresponding colors the experimentally determined values of J , J' and J'' for Cs_2CuCl_4 [11] and of J and J' for Cs_2CuBr_4 [15]. Additionally, the exchange coupling values are provided in Appendix D.

We first compare the Heisenberg models of Cs_2CuCl_4 , derived for the experimental as well as relaxed crystal structures [Figs. 8 (a)-(e)]. The common feature for all these structures is that their spin models are two-dimensional, with J being the leading interaction followed by J' .

For the experimental structure [Fig. 8 (b)], the ratio J'/J is similar to the experimentally determined ratio [11, 65], while the absolute values of J and J' , which are calculated in the present work, are off by a factor of almost 3. In this structure, the two-dimensionality is less pronounced due to the interlayer antiferromagnetic interaction J_3 and the ferromagnetic interaction J_7 , which are competing with J' . The GGA[nm] structure [Fig. 8 (e)], on the other hand, tends to behave as a 1D rather than 2D system as here the J'/J ratio is 0.15 at $U = 6$ eV. We assume that $U = 6$ eV should be close to the U value for the Cu $3d$ electrons in the LAPW GGA+U scheme (see, for instance, Ref. 66 where the authors successfully reproduce the electric field gradients at Cu^{2+} ions in a number of Cu^{2+} oxides and halides by performing LDA+U calculations with $U^{\text{eff}} = U - J = 5$ eV). The J'/J ratios at $U = 6$ eV in the experimental, GGA+U[fm] and GGA[fm] structures are, respectively, 0.30, 0.47 and 0.27. These ratios vary slightly for other U values.

The differences in the J'/J ratios among the relaxed structures are mainly due to a strong variation of the coupling J , which adopts the values 0.384, 0.568, 0.932 meV for $U = 6$ eV in the GGA+U[fm], GGA[fm] and GGA[nm] structures, respectively, whereas J' decreases only slightly for the same sequence of structures.

Judging by the proximity of the theoretically derived Cs_2CuCl_4 Heisenberg model (this work) to the experimentally determined one [11], the calculations with the GGA[fm] and GGA+U[fm] optimized structures provide the most satisfactory results. In both cases, the absolute values of J and J' as well as their ratios are close to experiment for typical values of U between 6 and 8 eV (for GGA+U[fm] $U \approx 6$ eV yields the best agreement, while in the case of GGA[fm] interpolation of the results

between 6 and 8 eV results in almost perfect agreement with experiment for $U \approx 7$ eV). Moreover we find non-negligible interlayer couplings as shown in Appendix D (bold-face values).

For the spin models calculated with the relaxed Cs_2CuCl_4 structures, the ratios of antiferromagnetic exchange couplings are in good agreement with the ratios of the corresponding squared hopping integrals. This is an indication that ferromagnetic contributions to these couplings are small.

In contrast to Cs_2CuCl_4 , the Cs_2CuBr_4 effective spin model derived using the experimental crystal structure [Fig. 8 (f)] agrees well with the experimentally estimated model parameters in the interval of U values around 6 eV. We obtain that Cs_2CuBr_4 is a two-dimensional system, with dominant antiferromagnetic couplings J and J' and considerably smaller interlayer couplings. At $U = 6$ eV, the obtained J'/J ratio equals 0.64, which compares well with the experimental result of 0.74. Also, the model based on the GGA+U[fm] relaxed structure [Fig. 8 (g)] gives similar results for the exchange parameters. The similarity between these two models is another feature that distinguishes Cs_2CuBr_4 from Cs_2CuCl_4 . In the latter case, as seen above, the exchange couplings of the experimental model [Fig. 8 (b)] are considerably smaller than those of the GGA+U[fm] relaxation model [Fig. 8 (c)].

Overall, the Heisenberg models for Cs_2CuBr_4 obtained within the GGA relaxation series [Figs. 8 (g)-(i)] follow the same behavior as the corresponding Cs_2CuCl_4 models, which is characterized by increasing J and decreasing J'/J in structures that have been relaxed with a smaller Cu magnetic moment.

To conclude this section, we briefly comment on the performance of the atomic limit (AL) version [54] of the GGA+U exchange-correlation functional, which is an alternative to the around mean field version. The exchange couplings of the experimental Cs_2CuCl_4 structure calculated with the AL double counting correction differ considerably from those obtained with the AMF double counting correction [compare panels (b) and (c) of Fig. 8]. The AL calculated exchange couplings J and J' do not behave linearly with $1/U$, as expected from the $J = 4t^2/U$ relation, valid for these antiferromagnetic couplings. Therefore, we restrict ourselves in the remaining discussion to calculations with the AMF double counting correction.

IV. DISCUSSION

From our analysis of the structural and electronic properties of Cs_2CuCl_4 and Cs_2CuBr_4 we obtained the following results: Within the sequence LDA[nm], GGA[nm], GGA[fm] and GGA+U[fm] of functionals used for the structural optimization, the Jahn-Teller-like distortion of

the CuX_4 tetrahedron is reduced, which is accompanied by an increase of the Cu-X(3)-X(3) angle α in the J superexchange path. These structural changes lead to a considerable variation of the exchange coupling J and the corresponding hopping integral t .

(a) Importance of magnetism and electronic correlations

We find that the choice of the functional used in the structure optimization is crucial for the correct modeling of the properties of these two compounds, especially in the case of Cs_2CuCl_4 . First of all, opening of a gap at the Fermi level by introducing various magnetic structures seems to be a necessary ingredient in the structure optimization, as can be seen from the relatively bad performance of the LDA[nm] and GGA[nm] optimizations. Since in these schemes the system is gapless, which is in stark contrast to the true ground state of Cs_2CuCl_4 observed experimentally, the strong instability at the Fermi level (visible in the peak in the DOS) has to be partially relieved by forcing an unphysically strong structural distortion, leading to an improper determination of lattice structure. Furthermore, a change of the size of the gap through onsite correlations and corresponding localization of the Cu magnetic moments also influences the results of the structure optimization. Although one might have expected a better performance of the spin-dependent optimization schemes (due to the magnetic nature of the compounds), the strong impact on the calculated exchange couplings is rather unexpected. The reason is presumably the small values of the exchange constants.

(b) Comments on the quality of the experimentally determined Cs_2CuCl_4 and Cs_2CuBr_4 crystal structures

Comparison of electronic behavior and effective models of the various relaxed Cs_2CuCl_4 structures with those of the experimental structure indicates that the experimental determination of the Cs_2CuCl_4 crystal structure [3] was probably not sufficiently accurate, at least, as far as calculations of microscopic models are concerned. This would explain the huge differences between our derived Cs_2CuCl_4 Heisenberg model when the experimental crystal structure is considered, and the model Coldea *et al.* [11] obtained from fitting to neutron data and which was corroborated by a number of studies [10, 19, 27, 69].

Accurate determination of the Cs_2CuCl_4 crystal structure might be complicated due to the presence of non-stoichiometric hydrogen containing compounds, presumably HCl or HO_2 , detected in this material and not detected in Cs_2CuBr_4 [3, 68].

The experimentally determined Cs_2CuBr_4 crystal structure, on the other hand, is accurate enough. We suggest therefore that Cs_2CuBr_4 can be regarded as a reference system for choosing the relaxation scheme, suitable also for describing Cs_2CuCl_4 . We conclude from the data analysis and from the physical considerations that such a relaxation scheme is the GGA[fm](GGA+U[fm]), with $0 \leq U \leq 6$ eV.

(c) Comparison with the experimentally determined microscopic models

In view of the arguments presented above, one should refer to the results obtained with either GGA[fm] or GGA+U[fm] relaxed structures when discussing the realistic spin model for Cs_2CuCl_4 . Our calculations confirm for both systems that their spin models are 2D, with the intraplane J and J' being the leading interactions, and Cs_2CuBr_4 showing a higher degree of frustration than Cs_2CuCl_4 . The model from Coldea *et al.* [11], with $J = 0.374$ eV and $J'/J = 0.34$, is close to our DFT models derived with the GGA[fm] and GGA+U[fm] relaxed structures and remains a valid model for Cs_2CuCl_4 . In Cs_2CuBr_4 , where the experimental crystal structure seems to be much more reliable, we can propose an approximate DFT model, obtained as a generalization of the models of Figs. 8 (f) and (g) for $U \approx 6$ eV: $0.8 \lesssim J \lesssim 0.9$, $0.5 \lesssim J'/J \lesssim 0.65$. This model is quite close to the model by Ono *et al.* [15], with $J = 0.97$ eV and $J'/J = 0.74$.

Additionally, in view of the recent theoretical studies by Starykh *et al.* [27, 69], who demonstrated the important role of the relatively weak Dzyaloshinskii-Moriya interaction and interlayer coupling in determining the magnetic behavior of Cs_2CuCl_4 , our results for the effective Cs_2CuCl_4 model reveal a possible relevance of a number of interlayer couplings, besides J'' , which are of comparable strength (J_1 , J_3 and J_7). Also, we find the next-nearest chain neighbor hopping integral t_{14} to be quite large, thus supporting another suggestion by these authors.

Finally, it is important to emphasize that the electronic TB models for the two compounds involve sizable interlayer hoppings, comparable with the intralayer ones, so that in terms of electronic degrees of freedom the two compounds have 3D behavior. In the case of Cs_2CuBr_4 , this can be seen from the large dispersion of the bands along the a^* direction in k -space, even though we didn't derive a TB model for this material.

(d) Structural relaxation

Finally, we comment on our decision to perform structural relaxations with fixed lattice constants and using

the room temperature data. It is generally known that the GGA tends to overestimate the unit cell volume while the LDA underestimates it. Therefore, we preferred to rely on the experimental lattice constants, which are usually determined with high accuracy. We performed a test GGA[nm] relaxation of the Cs_2CuCl_4 crystal structure with lattice constants measured at 0.3 K [11] and found that the electronic structure and the TB model of the resulting Cs_2CuCl_4 structure are close to the electronic structure and the TB model of the GGA[nm] Cs_2CuCl_4 structure, relaxed with the room temperature lattice constants. Therefore, all calculations have been performed with the room temperature lattice constants for both compounds.

V. SUMMARY AND CONCLUSIONS

In summary, we have performed DFT calculations for Cs_2CuCl_4 and Cs_2CuBr_4 . Our study shows that the exchange coupling constants of these compounds exhibit a strong dependence on subtle details of the crystal structure, especially on the geometry of the CuX_4 tetrahedra. Depending on the structural model, we observe a large variation of the derived exchange couplings and their ratios, resulting in completely different spin model Hamiltonians. One reason for this unusual sensitivity are the fairly small absolute values of the exchange couplings, with the largest coupling constant J being below 5 K.

One important motivation for our detailed study is the failure of the experimental structure published in Ref. 3 to correctly describe the magnetic behavior of Cs_2CuCl_4 . Calculations with the experimental structure provide too small exchange coupling constants with fairly strong interlayer couplings in contrast to the pronounced 2D character observed in experiment. This indicates (together with the fairly large forces acting on the atomic positions) that a better characterization of the Cs_2CuCl_4 crystal structure is necessary. Only after structural optimization with spin-dependent GGA and GGA+U functionals, we obtain an overall good agreement with the exchange couplings obtained from experiment [11].

In contrast, the leading exchange couplings for Cs_2CuBr_4 obtained from our calculations are in good agreement with those derived from experiment, independently of whether we use the experimental structure or structures from spin-resolved optimizations.

ACKNOWLEDGMENTS

We would like to thank W. Aßmus, F. Ritter, N. Krüger, M. Lang, B. Wolf, S.S. Saxena, Y. Tanaka, and O. A. Starykh for useful discussions. We gratefully acknowledge the Deutsche Forschungsgemeinschaft for financial support through the SFB/TRR 49 pro-

gram and the Helmholtz Association for support through HA216/EMMI.

APPENDIX A: STRUCTURAL PARAMETERS OF CS_2CUCL_4 AND CS_2CUBR_4 OBTAINED WITHIN DIFFERENT OPTIMIZATION SCHEMES

Below, we provide the Cs_2CuCl_4 and Cs_2CuBr_4 relative atomic positions obtained after structural optimization within different schemes. For a quick reference, we also cite Ref. 3 for the experimentally found structure of Cs_2CuCl_4 and Ref. 4 for that of Cs_2CuBr_4 .

In the case of Cs_2CuCl_4 , for the experimental structure and structures relaxed with non-spin-resolved and ferromagnetic calculations, the lattice constants are $a = 9.769 \text{ \AA}$, $b = 7.607 \text{ \AA}$, $c = 12.381 \text{ \AA}$ and the space group is $Pnma$. The structures relaxed with antiferromagnetic calculations (GGA[afm] and GGA+U[afm]), for which the relaxation was constrained by the symmetry of the $P21/c$ space group in a supercell, were found to eventually belong to the same space group $P21/c$ but in a reduced cell, with the same unit cell parameters as those of the original full-symmetry unit cell of the compound.

LDA[nm]

	x	y	z
Cs(1)	0.1322	0.25	0.1005
Cs(2)	0.9837	0.75	0.3287
Cu	0.2322	0.25	0.4149
Cl(1)	0.0115	0.25	0.3692
Cl(2)	0.3494	0.25	0.5697
Cl(3)	0.2824	0.9772	0.3654

GGA[nm]

	x	y	z
Cs(1)	0.1329	0.25	0.1050
Cs(2)	0.9864	0.75	0.3321
Cu	0.2320	0.25	0.4165
Cl(1)	0.0045	0.25	0.3751
Cl(2)	0.3507	0.25	0.5743
Cl(3)	0.2878	0.9779	0.3615

In the case of Cs_2CuBr_4 , the lattice constants are $a = 10.195 \text{ \AA}$, $b = 7.965 \text{ \AA}$, $c = 12.936 \text{ \AA}$ and the space group is $Pnma$.

GGA[fm]			
	x	y	z
Cs(1)	0.1318	0.25	0.1042
Cs(2)	0.9903	0.75	0.3308
Cu	0.2311	0.25	0.4178
Cl(1)	0.0039	0.25	0.3768
Cl(2)	0.3479	0.25	0.5764
Cl(3)	0.2918	0.9823	0.3588

GGA+U[fm]			
	x	y	z
Cs(1)	0.1321	0.25	0.1026
Cs(2)	0.9948	0.75	0.3302
Cu	0.2320	0.25	0.4175
Cl(1)	0.0043	0.25	0.3791
Cl(2)	0.3442	0.25	0.5779
Cl(3)	0.2961	0.9848	0.3556

GGA[afm]			
	x	y	z
Cs(1)	0.1317	0.2503	0.1044
Cs(2)	0.9899	0.7504	0.3309
Cu	0.2312	0.2502	0.4177
Cl(1)	0.0037	0.2497	0.3765
Cl(2)	0.3483	0.2507	0.5762
Cl(3a)	0.2912	0.5181	0.3591
Cl(3b)	0.2916	0.9823	0.3595

GGA+U[afm]			
	x	y	z
Cs(1)	0.1321	0.2501	0.1029
Cs(2)	0.9946	0.7501	0.3302
Cu	0.2319	0.2501	0.4175
Cl(1)	0.0037	0.2499	0.3790
Cl(2)	0.3446	0.2501	0.5777
Cl(3a)	0.2959	0.5151	0.3558
Cl(3b)	0.2959	0.9851	0.3557

Experimentally determined structure

	x	y	z
Cs(1)	0.1340	0.25	0.1031
Cs(2)	0.9433	0.75	0.3252
Cu	0.2302	0.25	0.4182
Cl(1)	0.0050	0.25	0.3820
Cl(2)	0.3433	0.25	0.5739
Cl(3)	0.2936	0.9881	0.3550

LDA[nm]

	x	y	z
Cs(1)	0.1244	0.25	0.1030
Cs(2)	0.0142	0.25	0.6638
Cu	0.2345	0.25	0.4159
Br(1)	0.0090	0.25	0.3715
Br(2)	0.3497	0.25	0.5751
Br(3)	0.2882	0.5267	0.3649

GGA[nm]

	x	y	z
Cs(1)	0.1272	0.25	0.1072
Cs(2)	0.0117	0.25	0.6619
Cu	0.2322	0.25	0.4168
Br(1)	0.0001	0.25	0.3756
Br(2)	0.3499	0.25	0.5787
Br(3)	0.2921	0.5257	0.3603

GGA[fm]

	x	y	z
Cs(1)	0.1260	0.25	0.1059
Cs(2)	0.0060	0.25	0.6628
Cu	0.2312	0.25	0.4187
Br(1)	-0.0002	0.25	0.3773
Br(2)	0.3456	0.25	0.5818
Br(3)	0.2977	0.5197	0.3570

GGA+U[fm]

	x	y	z
Cs(1)	0.1268	0.25	0.1044
Cs(2)	0.0030	0.25	0.6637
Cu	0.2326	0.25	0.4180
Br(1)	0.0004	0.25	0.3789
Br(2)	0.3435	0.25	0.5825
Br(3)	0.3004	0.5177	0.3542

Experimentally determined structure

	x	y	z
Cs(1)	0.1290	0.25	0.1058
Cs(2)	0.0049	0.25	0.6694
Cu	0.2311	0.25	0.4187
Br(1)	0.0010	0.25	0.3819
Br(2)	0.3440	0.25	0.5797
Br(3)	0.2960	0.5138	0.3546

APPENDIX B: FURTHER INTERACTION PATHWAYS IN CS_2CUCL_4 CONSIDERED IN THE TB MODEL

The interaction pathways for spin exchange coupling constants J_7 , J_6 , J_{14} , J_{18} and J_{22} are shown in Fig. 9 (a).

APPENDIX C: ANTIFERROMAGNETIC SPIN CONFIGURATIONS AND CORRESPONDING $E^{\text{FM}} - E^{\text{AFM}}$ EQUATIONS FOR DERIVING EXCHANGE CONSTANTS IN CS_2CUCL_4 AND CS_2CUBR_4

Given that the Cu atoms in the $2 \times 2 \times 1$ supercell of Cs_2CuCl_4 or Cs_2CuBr_4 are labeled as shown in Fig. 9 (b), the seven antiferromagnetic (or ferrimagnetic) spin configurations, considered in order to calculate exchange couplings J , J' , J''_{eff} , J_1 , J_3 , J_7 and J_8 by the total energy difference method, are the following:

	Cu1	Cu2	Cu3	Cu4	Cu5	Cu6	Cu7	Cu8
conf. 1:	↑	↓	↑	↓	↑	↓	↑	↓
conf. 2:	↓	↓	↑	↑	↑	↑	↓	↓
conf. 3:	↑	↑	↑	↑	↑	↑	↓	↓
conf. 4:	↑	↑	↑	↑	↓	↓	↓	↓
conf. 5:	↑	↓	↓	↑	↑	↓	↓	↑
conf. 6:	↓	↓	↑	↑	↓	↓	↑	↑
conf. 7:	↑	↓	↓	↓	↓	↑	↑	↑

Each of these spin configurations leads to a corresponding equation:

$$\begin{aligned}
 2J + 2J' &+ J_1 + J_3 + 4J_8 &= E_1/4, \\
 2J' + J''_{\text{eff}} &+ 2J_8 &= E_2/8, \\
 2J' + J''_{\text{eff}} + J_1 &+ 2J_8 + J_7 &= E_3/4, \\
 J''_{\text{eff}} + J_1 + J_3 + 2J_8 + 2J_7 &= E_4/4, \\
 2J + 2J' + J''_{\text{eff}} + J_1 + J_3 + 2J_8 + 2J_7 &= E_5/4, \\
 4J' + J''_{\text{eff}} + J_1 + J_3 + 2J_8 + 2J_7 &= E_6/4, \\
 4J + 8J' + 6J''_{\text{eff}} + 3J_1 + 3J_3 + 8J_8 + 4J_7 &= E_7,
 \end{aligned}$$

where $E_i = E^{\text{FM}} - E_i^{\text{AFM}}$, $i = 1, \dots, 7$, with E^{FM} being the energy of the supercell in the ferromagnetic configuration of Cu spins and E_i^{AFM} being the energy of the supercell in the antiferromagnetic configuration i .

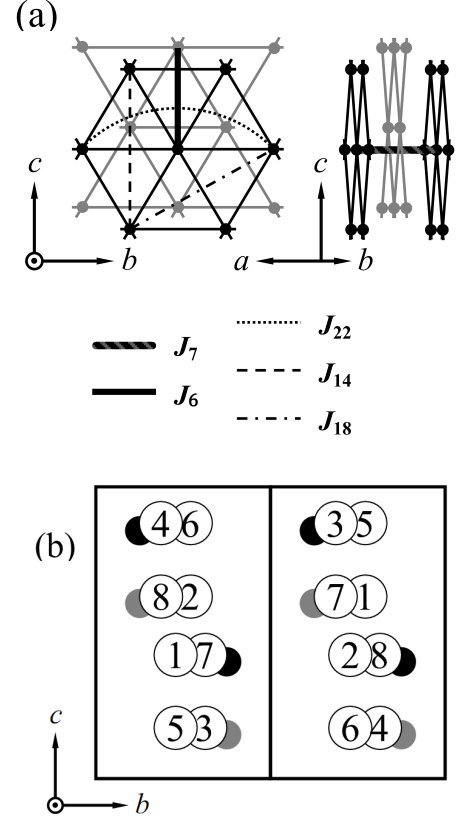


FIG. 9: (a) Interaction pathways J_7 , J_6 , J_{14} , J_{18} and J_{22} . (b) Labeling of the Cu atoms in the $2 \times 2 \times 1$ supercell of Cs_2CuCl_4 or Cs_2CuBr_4 . The black and gray circles denote Cu atoms that belong to adjacent Cu layers, parallel to the bc plane. Since the supercell contains two unit cells along the a axis, the black and gray Cu lattices are doubled, which is not visible in the bc projection. The two encircled figures, one on top of the other, label the Cu atoms that have common y and z coordinates, but whose x coordinates differ by the lattice constant a such that the top figure refers to the Cu atom with larger x coordinate.

APPENDIX D: EXCHANGE COUPLINGS

The exchange couplings provided below for the experimental as well as the GGA[nm], GGA[fm] and GGA+U[fm] relaxed Cs_2CuCl_4 and Cs_2CuBr_4 crystal structures are given in meV. We have marked in bold face the parameter values that should provide a realistic description of the spin models for Cs_2CuCl_4 and Cs_2CuBr_4 .

Cs₂CuCl₄: experimental structure [Fig. 8 (b)]

	$U=4$ eV	$U=6$ eV	$U=8$ eV
J	0.2170	0.1128	0.0413
J'	0.0548	0.0333	0.0169
J''_{eff}	0.0112	0.0061	0.0048
J_1	0.0085	-0.0039	-0.0046
J_3	0.0229	0.0160	0.0070
J_8	0.0057	0.0035	0.0018
J_7	-0.0152	-0.0081	-0.0030

Cs₂CuBr₄: experimental structure [Fig. 8 (f)]

	$U=4$ eV	$U=6$ eV	$U=8$ eV
J	1.6597	0.7911	0.2756
J'	1.0427	0.5064	0.2030
J''_{eff}	0.0868	0.0336	0.0127
J_1	0.1525	0.0516	0.0143
J_3	0.0675	0.0599	0.0273
J_8	-0.0147	-0.0002	0.0019
J_7	-0.0266	-0.0116	-0.0040

Cs₂CuCl₄: GGA+U[fm] relaxed structure [Fig. 8 (c)]

	$U=4$ eV	$U=6$ eV	$U=8$ eV
J	0.8517	0.3837	0.1385
J'	0.3736	0.1788	0.0779
J''_{eff}	0.0266	0.0137	0.0089
J_1	0.0210	0.0039	0.0010
J_3	0.0008	0.0147	0.0046
J_8	-0.0039	-0.0005	0.0011
J_7	-0.0219	-0.0172	-0.0065

Cs₂CuBr₄: GGA+U[fm] relaxed structure [Fig. 8 (g)]

	$U=4$ eV	$U=6$ eV	$U=8$ eV
J	2.0358	0.9282	0.3019
J'	1.0223	0.4821	0.1815
J''_{eff}	0.0589	0.0238	0.0105
J_1	0.1268	0.0436	0.0119
J_3	0.0685	0.0694	0.0307
J_8	-0.0142	-0.0011	0.0012
J_7	-0.0368	-0.0204	-0.0086

Cs₂CuCl₄: GGA[fm] relaxed structure [Fig. 8 (d)]

	$U=4$ eV	$U=6$ eV	$U=8$ eV
J	1.2632	0.5679	0.2095
J'	0.3207	0.1556	0.0702
J''_{eff}	0.0224	0.0175	0.0118
J_1	0.0308	0.0127	0.0031
J_3	0.0435	0.0302	0.0108
J_8	-0.0043	-0.0010	0.0011
J_7	-0.0222	-0.0172	-0.0067

Cs₂CuBr₄: GGA[fm] relaxed structure [Fig. 8 (h)]

	$U=4$ eV	$U=6$ eV	$U=8$ eV
J	2.7229	1.2325	0.4076
J'	0.9234	0.4382	0.1682
J''_{eff}	0.0554	0.0219	0.0122
J_1	0.1467	0.0492	0.0166
J_3	0.1710	0.1101	0.0468
J_8	-0.0158	-0.0005	0.0004
J_7	-0.0394	-0.0183	-0.0089

Cs₂CuCl₄: GGA[nm] relaxed structure [Fig. 8 (e)]

	$U=4$ eV	$U=6$ eV	$U=8$ eV
J	2.1036	0.9321	0.3440
J'	0.2873	0.1418	0.0656
J''_{eff}	0.0076	0.0089	0.0112
J_1	0.0424	0.0150	0.0061
J_3	0.0919	0.0468	0.0185
J_8	-0.0047	0.0006	0.0010
J_7	-0.0247	-0.0138	-0.0065

Cs₂CuBr₄: GGA[nm] relaxed structure [Fig. 8 (i)]

	$U=4$ eV	$U=6$ eV	$U=8$ eV
J	5.1309	2.2669	0.7423
J'	0.8025	0.3872	0.1540
J''_{eff}	0.0356	0.0129	0.0115
J_1	0.1980	0.0696	0.0246
J_3	0.3723	0.1907	0.0741
J_8	-0.0196	-0.0015	0.0011
J_7	-0.0521	-0.0190	-0.0083

[1] R. Coldea, D. A. Tennant, R. A. Cowley, D. F. McMorrow, B. Dorner and Z. Tylczynski, J. Phys.: Condens. Matter **8**, 7473 (1996).

- [2] H. Tanaka, T. Ono, H. Aruga Katori, H. Mitamura, F. Ishikawa and T. Goto, Prog. Theor. Phys. Suppl. **145**, 101 (2002)
- [3] S. Bailleul, D. Svoronos, P. Porcher, and A. Tomas, Comptes Rendus Hebdomadaires des Seances de l'Academie des Sciences **313**, 1149 (1991).
- [4] B. Morosin and E. C. Lingafelter, Acta Cryst. **13**, 807 (1960).
- [5] R. Coldea, D. A. Tennant and Z. Tylczynski, Phys. Rev. B **68**, 134424 (2003).
- [6] Y. Tokiwa, T. Radu, R. Coldea, H. Wilhelm, Z. Tylczynski and F. Steglich, Phys. Rev. B **73**, 134414 (2006).
- [7] T. Ono, H. Tanaka, H. Aruga Katori, F. Ishikawa, H. Mitamura and T. Goto, Phys. Rev. B **67**, 104431 (2003).
- [8] T. Ono *et al.*, Prog. Theor. Phys. Suppl. **159**, 217 (2005).
- [9] H. Tsujii, C. R. Rotundu, T. Ono, H. Tanaka, B. Andraka, I. Ingersent and Y. Takano, Phys. Rev. B **76**, 060406(R) (2007).
- [10] W. Zheng, R. R. P. Singh, R. H. McKenzie and R. Coldea, Phys. Rev. B **71**, 134422 (2005).
- [11] R. Coldea, D. A. Tennant, K. Habicht, P. Smeibidl, C. Wolters, and Z. Tylczynski, Phys. Rev. Lett. **88**, 137203 (2002).
- [12] I. Dzyaloshinskii, J. Phys. Chem. Solids **4**, 241 (1958).
- [13] T. Moriya, Phys. Rev. **120**, 91 (1960).
- [14] Z. Weihong, R. H. McKenzie, and R. P. Singh, Phys. Rev. B **59**, 14367 (1999).
- [15] T. Ono, H. Tanaka, T. Nakagomi, O. Kolomiyets, H. Mitamura, F. Ishikawa, T. Goto, K. Nakajima, A. Oosawa, Y. Koike, K. Kakurai, J. Klenke, P. Smeibidle, M. Meissner and H. Aruga Katori, J. Phys. Soc. Jpn. **74**, Suppl. 135 (2005).
- [16] Y. Zhou and X.-G. Wen, cond-mat/0210662v2.
- [17] S. Yunoki and S. Sorella, Phys. Rev. Lett. **92**, 157003 (2004).
- [18] J. Alicea, O. I. Motrunich, and M. P. A. Fisher, Phys. Rev. Lett. **95**, 247203 (2005).
- [19] M. Y. Veillette, A. J. A. James, and F. H. L. Essler, Phys. Rev. B **72**, 134429 (2005).
- [20] S. V. Isakov, T. Senthil, and Y. B. Kim, Phys. Rev. B **72**, 174417 (2005).
- [21] W. Zheng, J. O. Fjaerestad, R. R. P. Singh, R. H. McKenzie, and R. Coldea, Phys. Rev. Lett. **96**, 057201 (2006).
- [22] D. Dalidovich, R. Sknepnek, A. J. Berlinsky, J. Zhang, and C. Kallin, Phys. Rev. B **73**, 184403 (2006).
- [23] M. Q. Weng, D. N. Sheng, Z. Y. Weng, and R. J. Bursill, Phys. Rev. B **74**, 012407 (2006).
- [24] S. Yunoki and S. Sorella, Phys. Rev. B **74**, 014408 (2006).
- [25] J. O. Fjaerestad, W. Zheng, R. R. P. Singh, R. H. McKenzie, and R. Coldea, Phys. Rev. B **75**, 174447 (2007).
- [26] M. Kohno, O. A. Starykh and L. Balents, Nature Physics **3**, 790 (2007).
- [27] O. A. Starykh and L. Balents, Phys. Rev. Lett. **98**, 077205 (2007).
- [28] J. Alicea and M. P. A. Fisher, Phys. Rev. B **75**, 144411 (2007).
- [29] J. Alicea, A. V. Chubukov, and O. A. Starykh, Phys. Rev. Lett. **102**, 137201 (2009).
- [30] N. A. Fortune, S. T. Hannahs, Y. Yoshida, T. E. Sherline, T. Ono, H. Tanaka, and Y. Takano, Phys. Rev. Lett. **102**, 257201 (2009).
- [31] M. Kohno, Phys. Rev. Lett. **103**, 197203 (2009).
- [32] D. Heidarian, S. Sorella, and F. Becca, Phys. Rev. B **80**, 012404 (2009).
- [33] C. Xu and S. Sachdev, Phys. Rev. B **79**, 064405 (2009).
- [34] R. F. Bishop, P. H. Y. Li, D. J. J. Farnell, and C. E. Campbell, Phys. Rev. B **79**, 174405 (2009).
- [35] D. J. Singh and M.-H. Du, Phys. Rev. Lett. **100**, 237003 (2008).
- [36] I. I. Mazin, M. D. Johannes, L. Boeri, K. Koepernik, and D. J. Singh, Phys. Rev. B **78**, 085104 (2008).
- [37] M. J. Han, Q. Yin, W. E. Pickett, and S. Y. Savrasov, Phys. Rev. Lett. **102**, 107003 (2009).
- [38] Z. P. Yin, S. Lebegue, M. J. Han, B. P. Neal, S. Y. Savrasov, and W. E. Pickett, Phys. Rev. Lett. **101**, 047001 (2008).
- [39] I. Opahle, H. C. Kandpal, Y. Zhang, C. Gros, and R. Valentí, Phys. Rev. B **79**, 024509 (2009).
- [40] Y.-Z. Zhang, H. C. Kandpal, I. Opahle, H. O. Jeschke, and R. Valentí, Phys. Rev. B **80**, 094530 (2009).
- [41] Y.-Z. Zhang, I. Opahle, H. O. Jeschke, and R. Valentí, Phys. Rev. B **81**, 094505 (2010).
- [42] L. Pisani and R. Valentí, Phys. Rev. B **71**, 180409 (2005).
- [43] L. Pisani, R. Valentí, B. Montanari and N. M. Harrison, Phys. Rev. B **76**, 235126 (2007).
- [44] Y.-Z. Zhang, H. O. Jeschke, and R. Valentí, Phys. Rev. B **78**, 205104 (2008).
- [45] D. Mastrogiuseppe and A. Dobry, Phys. Rev. B **79**, 134430 (2009).
- [46] Y.-Z. Zhang, H. O. Jeschke, and R. Valentí, Phys. Rev. Lett. **101**, 136406 (2008).
- [47] S. Blanco-Canosa, F. Rivadulla, A. Pineiro, V. Pardo, D. Baldomir, D. I. Khomskii, M. M. Abd-Elmeguid, M. A. Lopez-Quintela, and J. Rivas, Phys. Rev. Lett. **102**, 056406 (2009).
- [48] A. Prodi, J. S. Helton, Y. Feng, and Y.S. Lee, Phys. Rev. B **81**, 201103(R) (2010).
- [49] Y.-Z. Zhang, K. Foyevtsova, H. O. Jeschke, M. U. Schmidt, and R. Valentí, Phys. Rev. Lett. **104**, 146402 (2010).
- [50] M. Sing, S. Glawion, M. Schlachter, M. R. Scholz, K. Goss, J. Heidler, R. Claessen, arXiv:0905.1381.
- [51] Y.-Z. Zhang, I. Opahle, H. O. Jeschke, and R. Valentí, J. Phys.: Condens. Matter **22** (2010) 164208.
- [52] J. P. Perdew and Y. Wang, Phys. Rev. B **45**, 13244 (1992).
- [53] J. P. Perdew, K. Burke and M. Ernzerhof, Phys. Rev. Lett. **77**, 3865 (1996).
- [54] V. I. Anisimov, I. V. Solovyev, M. A. Korotin, M. T. Czyzyk and G. A. Sawatzky, Phys. Rev. B **48**, 16929 (1993).
- [55] H. Eschrig, K. Koepernik, and I. Chaplygin, J. Solid State Chemistry **176**, 482 (2003).
- [56] M. T. Czyzyk and G. A. Sawatzky, Phys. Rev. B **49**, 14211 (1994).
- [57] R. Coldea, D. A. Tennant, A. M. Tselik and Z. Tylczynski, Phys. Rev. Lett. **86**, 1335 (2001).
- [58] Note however that the definition of local site moments is not unique and may vary to some degree between different band structure codes.
- [59] Blaha P, Schwarz K, Madsen G K H, Kvasnicka D and Luitz J 2001 *WIEN2k, An Augmented Plane Wave + Local Orbitals Program for Calculating Crystal Properties* (Karlheinz Schwarz, Techn. Universität Wien, Austria) ISBN 3-9501031-1-2.
- [60] O. K. Andersen and T. Saha-Dasgupta, Phys. Rev. B **62**, R16219 (2000).
- [61] K. Koepernik and H. Eschrig, Phys. Rev. B **59**, 1743

- (1999).
- [62] J. B. Goodenough, *J. Phys. Chem. Solids* **6**, 287 (1958).
- [63] J. Kanamori, *J. Phys. Chem. Solids* **10**, 87 (1959).
- [64] J. Kuneš, W. Ku and W. E. Pickett, *J. Phys. Soc. Jpn.* **74**, 1408 (2005).
- [65] K. Foyevtsova, Y. Zhang, H. O. Jeschke and R. Valentí, *Jour. of Physics: Conf. Series* **145** 012038 (2009).
- [66] H. Haas and J. G. Correia, *Hyperfine Interactions* **176**, 9 (2007).
- [67] <http://www.FPLO.de>
- [68] N. Krüger, F. Ritter and W. Aßmus, private communication (2010).
- [69] O. A. Starykh, H. Katsura and L. Balents, *Phys. Rev. B* **82**, 014421 (2010).